

# Spin-up of low mass classical bulges in barred galaxies

Kanak Saha<sup>\*</sup>, Inma Martinez-Valpuesta & Ortwin Gerhard

*Max-Planck-Institut für Extraterrestrische Physik, Giessenbachstrae, D-85748 Garching, Germany*

Accepted xxxx Month xx. Received xxxx Month xx; in original form 2011 Nov. 24

## ABSTRACT

Secular evolution is one of the key routes through which galaxies evolve along the Hubble sequence. Not only the disk undergoes morphological and kinematic changes, but also a preexisting classical bulge may be dynamically changed by the secular processes driven primarily by the bar. We study the influence of a growing bar on the dynamical evolution of a low mass classical bulge such as might be present in galaxies like the Milky Way. Using self-consistent high resolution  $N$ -body simulations, we study how an initially isotropic non-rotating small classical bulge absorbs angular momentum emitted by the bar. The basic mechanism of this angular momentum exchange is through resonances and a considerable fraction of the angular momentum is channeled through Lagrange point (-1:1) and ILR (2:1) orbits. In the phase of rapid dynamical growth, also retrograde non-resonant orbits absorb significant angular momentum. As a result of this angular momentum gain, the initially non-rotating classical bulge transforms into a fast rotating, radially anisotropic and triaxial object, embedded in the similarly fast rotating boxy bulge formed from the disk. Towards the end of the evolution, the classical bulge develops cylindrical rotation. By that time, its inner regions host a "classical bulge-bar" whose distinct kinematics could serve as direct observational evidence for the secular evolution in the galaxy. Some implications of these results are discussed briefly.

**Key words:** galaxies: bulges – galaxies: structure – galaxies: kinematics and dynamics – galaxies: spiral – galaxies: evolution

## 1 INTRODUCTION

In the hierarchical structure formation scenario (White & Rees 1978; Fall & Efstathiou 1980) mergers have played a strong role in forming and shaping galaxies. One of the common product of major mergers are the classical bulges (Kauffmann et al. 1993; Baugh et al. 1996; Hopkins et al. 2009) which are the central building blocks in spiral galaxies. There have been a couple of other mechanisms suggested for the formation and growth of classical bulges e.g., monolithic collapse of primordial gas clouds (Eggen et al. 1962), the coalescence of giant clumps in gas-rich primordial galaxies (Immeli et al. 2004; Elmegreen et al. 2008), multiple minor mergers (Bournaud et al. 2007; Hopkins et al. 2010), accretion of small companions or satellites (Aguerre et al. 2001). The classical bulges formed via these processes seem to have little rotation as compared to the random motion. On the other hand, various observational measurements have confirmed that classical bulges in spiral galaxies possess rotation (Kormendy & Illingworth 1982; Cappellari et al. 2007) about their minor axis and in most cases in the same

sense as the disk rotates. It is also known that classical bulges rotate faster than elliptical galaxies and that often their rotation velocities are comparable to that of an isotropic oblate rotator model (Binney 1978). So the origin of the systematic rotational motion observed in the classical bulges remains unclear.

The photometric and kinematic properties of classical bulges as well as their origin are quite distinct from those of the other class of bulges, the boxy/peanut and disk-like bulges. It is well known that the surface brightness profiles in classical bulges follow a sersic law  $\mu(r) \sim r^{1/n}$  with sersic index  $n \sim 4$ . Whereas the sersic indices in boxy and disk-like bulges are, in general, low with  $n \lesssim 2$ ; so that their surface brightness profiles follow roughly an exponential distribution, see Kormendy & Kennicutt (2004); Combes (2009) for extensive reviews. The kinematics of bulges are well illustrated in the  $v/\sigma - \epsilon$  plot (Kormendy & Illingworth 1982; Kormendy 1982) which clearly demonstrates the distinction in the kinematic properties of ellipticals, classical bulges and boxy bulges and brings out the fact that in terms of their rotational support, classical bulges fall in between ellipticals and boxy/disk-like bulges. Since the boxy as well as disk-like bulges are thought to have formed from disk material, the source of their angular momentum is known.

<sup>\*</sup> E-mail: saha@mpe.mpg.de

The classical bulges formed early through major mergers and violent relaxation can subsequently accrete material quiescently as a result of which a disk grows inside-out (Mo et al. 1998; Katz et al. 2003; Springel & Hernquist 2005; Kereš et al. 2009). The gas accretion may facilitate the disk to grow sufficiently for the disk self-gravity to dominate the internal dynamics. Eventually, a bar and/or spiral arms form in the disk and initiate secular processes in the galaxy. Indeed, bars are quite common in disk galaxies, about 2/3 of the disk galaxies host a strong stellar bar in their central region (Laurikainen et al. 2004; Marinova & Jogee 2007; Menéndez-Delmestre et al. 2007). Therefore one might expect the disk to go bar unstable also in galaxies with pre-existing classical bulges. In fact, classical, boxy and disk-like bulges could co-exist (Athanasoula 2005; Erwin 2008; Gadotti 2009; Nowak et al. 2010) in a single galaxy, although the observational identification of the several components could be difficult. In the Milky Way, an upper limit on the mass of a classical bulge ( $\sim 8\%$  of the disk mass) has been set by modelling the kinematics from the Bulge Radial Velocity Assay (BRAVA) data (Shen et al. 2010). But there is evidence for a metallicity gradient above the Galactic plane (Zoccali et al. 2008; Zoccali 2010) which is taken as an indication for the existence of a classical bulge in our Galaxy. It is therefore important to understand the dynamical interaction between preexisting classical bulges and bars in barred galaxies.

In this paper, we investigate in considerable detail the interaction of a bar and a low mass classical bulge via a high resolution  $N$ -body simulation of a galaxy consisting of a live disk, bulge and dark matter halo, and follow the evolution of the dynamical structure and kinematics of the small classical bulge. We find that its dynamical evolution is strongly connected to the growth of the bar which forms spontaneously in the disk. During the secular evolution, the structure and kinematics of the bulge are altered significantly, developing an interesting and complex rotation structure; in particular, cylindrical rotation (which is considered as a typical proxy of boxy bulge) appears in the inner region of the classical bulge.

The paper is organized as follows. Section 2 summarizes the basics of bar-bulge interaction. Section 3 outlines the initial galaxy model and set up for the  $N$ -body simulation. The bar evolution and boxy bulge formation are described in Section 4. Section 5 describes, in detail, the angular momentum exchange between the bar and the classical bulge. The evolution of the classical bulge, its structure and kinematics are presented in Section 6. Discussion and conclusions are contained in Sections 7 and 8 respectively. In the text, by bulge, we mean a classical bulge unless mentioned otherwise.

## 2 BAR-BULGE INTERACTION

As we have seen (in Section 1), the possible co-existence of a bar and a classical bulge might be rather common in present day disk galaxies, and thus they are bound to interact gravitationally. In fact, a preexisting classical bulge in the disk has a strong influence on the formation and growth of the bar itself. For the swing amplification to work, one needs to keep alive the feedback loop through which a set of trailing waves traveling through the center are transformed

into leading waves. This is possible as long as there is no inner Lindblad resonances (ILRs). A highly centrally concentrated bulge can shield the center by putting an ILR barrier and thus cutting the feedback loop which in turn could hinder the growth of the bar (Sellwood & Evans 2001). However, various non-linear processes are probably active in real galaxies which would destroy the ILR barrier and eventually lead to the formation of a bar (Widrow et al. 2008; Dubinski et al. 2009).

Once a bar is formed, it takes over the dynamics in the central region of the disk and starts interacting with the stellar bulge and dark matter halo through exchange of angular momentum. Based on the work of Lynden-Bell & Kalnajs (1972), hereafter LKB72, it has been emphasized by several authors (Tremaine & Weinberg 1984; Weinberg 1985; Hernquist & Weinberg 1992; Debattista & Sellwood 2000; Weinberg & Katz 2002; Athanasoula 2002; Sellwood & Debattista 2006; Dubinski et al. 2009) that the resonant interaction plays a significant role in the angular momentum transfer between the bar and the dark matter halo. It has been suggested by Hernquist & Weinberg (1992); Athanasoula (2003); Weinberg & Katz (2007a) that the same underlying mechanism could as well apply between the bar and the spheroid and in particular, Athanasoula & Misiriotis (2002) have studied how the shape of a bulge would change in response to a growing bar.

Although the dynamical interaction between a growing bar and a bulge and their subsequent evolution can be best studied via  $N$ -body simulations, an analytic understanding is required to complement this. Following LKB72, it can be shown that during the bar-bulge interaction the time rate of change of angular momentum of a classical bulge, whose distribution function ( $F_b$ ) is described by a King model, is always positive and can be written as

$$\dot{L}_{z,b} \sim \Omega_B \times |\psi_{lmn}|^2 \times F_b / \sigma_b^2 > 0, \quad (1)$$

where  $\psi_{lmn}$  and  $\Omega_B$  are the Fourier amplitude and pattern speed of a non-responsive bar potential and  $\sigma_b$  is the velocity dispersion of the bulge stars. So at a given resonance, the angular momentum gained by the bulge depends on the strength of the bar and is inversely proportional to the square of bulge velocity dispersion, implying a hotter bulge will absorb less angular momentum provided other conditions remain unchanged. However, in real galaxies, the angular momentum transfer is more difficult to determine, because the time rate of change of bar's angular momentum involves the change in its pattern speed, moment of inertia, and in the angular momentum associated with any internal circulation (Villa-Vargas et al. 2009) within the bar. In Section 5, we show the angular momentum transfer between the bar and the bulge in our simulation using orbital spectral analysis.

## 3 GALAXY MODEL AND $N$ -BODY SIMULATION

An equilibrium model for a disk galaxy is constructed using the self-consistent bulge-disk-halo model of Kuijken & Dubinski (1995). Their prescription provides nearly exact solutions of the collisionless Boltzmann and

Poisson equations which are suitable for studying disk stability related problems. All the components in our model are live (i.e., the gravitational potential of each component can respond to an external or internal perturbation) and, hence, provide a realistic representation for the structure and evolution of the galaxy. Below we briefly describe each component of the model. For more details, the reader is referred to Kuijken & Dubinski (1995).

The disk distribution function is constructed using the approximate third integral given by  $E_z = \frac{1}{2}v_z^2 + \Psi(R, z) - \Psi(R, 0)$ , the energy of the vertical oscillations. This third integral is approximately conserved for orbits near the disk mid-plane. The radial density of the disk is approximately exponential with a truncation, and the square of the radial velocity dispersion follows the same exponential radial decline with a scale length same as the disc scale length. The vertical structure of the disk is approximately isothermal, with the scale height set by the vertical velocity dispersion and vertical potential gradient. The volume density of the axisymmetric disk is given by

$$\rho_d(R, z) = \frac{M_d}{8\pi h_z R_d^2} e^{-R/R_d} \operatorname{erfc}\left(\frac{R - R_{out}}{\sqrt{2}(R_{out} - R_{trun})}\right) f_d(z), \quad (2)$$

where  $f_d(z) = \exp(-0.8676\Psi_z(R, z)/\Psi_z(R, h_z))$  with  $\Psi_z(R, z) = \Psi(R, z) - \Psi(R, 0)$  governs the vertical structure of the disk,  $\operatorname{erfc}$  is the complementary error function. In the above equation,  $M_d$  is the disk mass,  $R_d$  is the scale length and  $h_z$  is the scale height.

A spherical live classical bulge is constructed from the King model (King 1966) and the corresponding distribution function (DF) is given by (Binney & Tremaine 1987)

$$f_b(E) = \begin{cases} \rho_b (2\pi\sigma_b^2)^{-3/2} e^{(\Psi_{b0} - \Psi_c)/\sigma_b^2} \\ \times \{e^{-(E - \Psi_c)/\sigma_b^2} - 1\} & \text{if } E < \Psi_c, \\ 0 & \text{otherwise.} \end{cases} \quad (3)$$

Here, the bulge is specified by three parameters, namely the cut-off potential ( $\Psi_c$  which determines the bulge tidal radius), central bulge density ( $\rho_b$ ) and central bulge velocity dispersion ( $\sigma_b$ ). The gravitational potential at the centre of the bulge is measured by  $\Psi_{b0}$ .

An axisymmetric live dark matter halo is constructed using the distribution function of a lowered Evans model (Evans 1993) and is given as

$$f_{dm}(E, L_z^2) = \begin{cases} [(AL_z^2 + B)e^{-E/\sigma_h^2} + C] \\ \times (e^{-E/\sigma_h^2} - 1) & \text{if } E < 0, \\ 0 & \text{otherwise.} \end{cases} \quad (4)$$

The halo is parameterized by a potential depth ( $\Psi_0$ ), velocity ( $\sigma_h$ ) and density scales ( $\rho_1$ ), a core radius  $R_c$  and the flattening parameter  $q$ . The factors  $A, B$ , and  $C$  are functions of these parameters (see Kuijken & Dubinski 1995 and references therein). The halo has a tidal radius specified by  $E = 0$ .

The total mass and the outer radii of both the bulge and halo are calculated in an iterative procedure. The potential is computed self-consistently by solving the Poisson equation for the combined three component system in an iterative fashion. First, the densities for the bulge and halo are obtained from their respective distribution function and then the disk density is added to it and the corresponding potential for the combined mass distribution is used as a

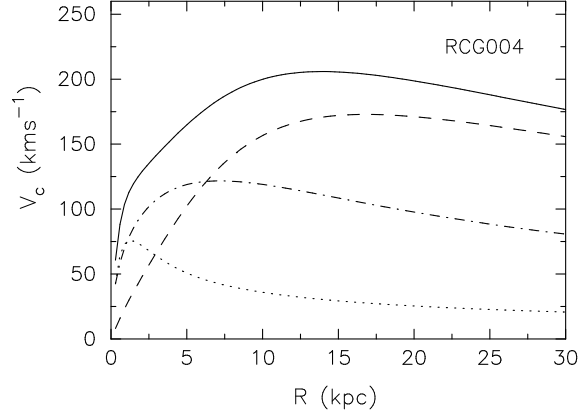


**Figure 1.** Initial circular velocity curve for the model galaxy. Solid line represents the total circular velocity. Dotted line is for the bulge, dashed line for the dark matter halo and dashed-dot dash for the disc.

starting point for carrying out the next iteration. We use a maximum of  $l = 10$  in the potential harmonic expansion and the iteration is continued until the outer radii for the bulge and halo are unchanged between successive iterations. The outer radii of the bulge and the halo correspond to the respective tidal radii. The masses of the bulge and halo correspond to the total mass enclosed within their respective outer radii computed by integrating the density profiles.

In this paper, we present the analysis of a particular galaxy model hosting a low mass classical bulge. For historical reasons, we call this model RCG004. The circular velocity curve for the model is presented in Fig 1. The length, mass and velocity units for this model are given by  $L = 4.0$  kpc,  $M = 2.33 \times 10^{10} M_\odot$  and  $V = 157$   $\text{kms}^{-1}$ . The disk outer radius ( $R_{out}$ ) is fixed at about  $6.5R_d$  and a truncation width  $\sim 0.3R_d$  is adopted within which the disk density smoothly decreases to zero at the outer radius. The disk scale length ( $R_d$ ) is fixed at 4.0 kpc and the scale height is 42 pc, the disk mass  $M_d = 4.5 \times 10^{10} M_\odot$ . The central value of the radial velocity dispersion is  $78.5$   $\text{kms}^{-1}$ . The Toomre Q profile is nearly flat in the radial range 0.5 to 5 scale lengths while it increases on either side of the disc. The Q value at the disc half mass radius is 1.4. The bulge mass  $M_b = 3 \times 10^9 M_\odot$ . In table 1, we quote the outer radius for the classical bulge (denoted by  $R_b$ ) in our galaxy model. The halo has a flattening of  $q = 0.8$  and a core radius  $R_c = 0.25$  kpc and a mass of  $M_h = 1.82 \times 10^{11} M_\odot$  within about 60 kpc.

We evolve the galaxy model in isolation to examine the evolution of the bulge shape, morphology and kinematics. The simulation is performed using the Gadget code (Springel et al. 2001) which uses a variant of the leapfrog method for the time integration. The forces between the particles are calculated using the Barnes & Hut (BH) tree with some modification (Springel et al. 2001) with a tolerance parameter  $\theta_{tol} = 0.7$ . The integration time step is  $\sim 0.4$  Myr and the model is evolved for 2.2 Gyr. For reference, the orbital time at the disk half mass radius is  $\sim 296$  Myr. A total of  $1.0 \times 10^7$  particles is used to simulate the model galaxy. The softening lengths for the disk, bulge and halo particles are 12, 40 and 36 pc respectively. The masses for the disk, bulge and halo particles are  $1.2 \times 10^4 M_\odot$ ,  $0.3 \times 10^4 M_\odot$  and  $3.6 \times 10^4 M_\odot$  respectively. To examine the effect of unequal

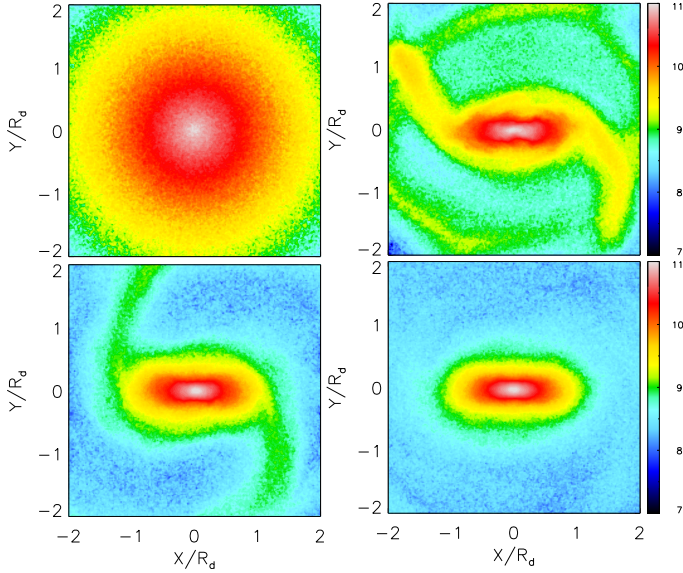


**Figure 2.** Surface density maps for the disk particles alone. Top left: density map at  $T=0$  Gyr, showing the axisymmetric disk. Top right: Same at  $T=0.56$  Gyr. Bottom left: at  $T=1.1$  Gyr and Bottom right: at  $T=2.1$  Gyr.

**Table 1.** Initial parameters for the model galaxy.

Galaxy model	$Q$	$B/D$	$B/T$	$\sigma_{b0}$ ( $\text{kms}^{-1}$ )	$R_b$ (kpc)
RCG004	1.40	0.0666	0.01306	65.0	6.08

$B/D$  is the bulge-to-disk mass ratio,  $B/T$  is the bulge-to-total (including dark halo mass) mass ratio,  $\sigma_{b0}$  is the bulge central velocity dispersion, and finally  $R_b$  is the outer radius of the bulge.

softenings, we have re-run the simulation with new softening parameters as prescribed by McMillan & Dehnen (2007). We note that with the new softenings, the bar growth is delayed by  $\sim 90$  Myr while the main results remain unchanged. The total energy is conserved within 0.2% till the end of the simulation. The total angular momentum is conserved within 3% at 2.2 Gyr for both the runs having different softening parameters.

#### 4 BAR AND BOXY BULGE

Although it is not clearly understood how bars are formed in real galaxies, swing amplification (Toomre 1981) plays a significant role in making an initially axisymmetric, equilibrium model of a disk galaxy bar unstable (Sellwood 1981). Once formed,  $N$ -body bars are found to be long-lived, dominate the disk dynamics, and are responsible for driving secular evolution processes in the galaxy (Sellwood & Wilkinson 1993). Fig. 2 depicts the formation and evolution of the bar from the initially axisymmetric disk. Strong two-armed spirals are also formed along with the bar and last till 1.1 Gyr in our simulation. The ring-like structure at  $T = 0.56$  Gyr is intersecting the spiral arms indicating that it is probably

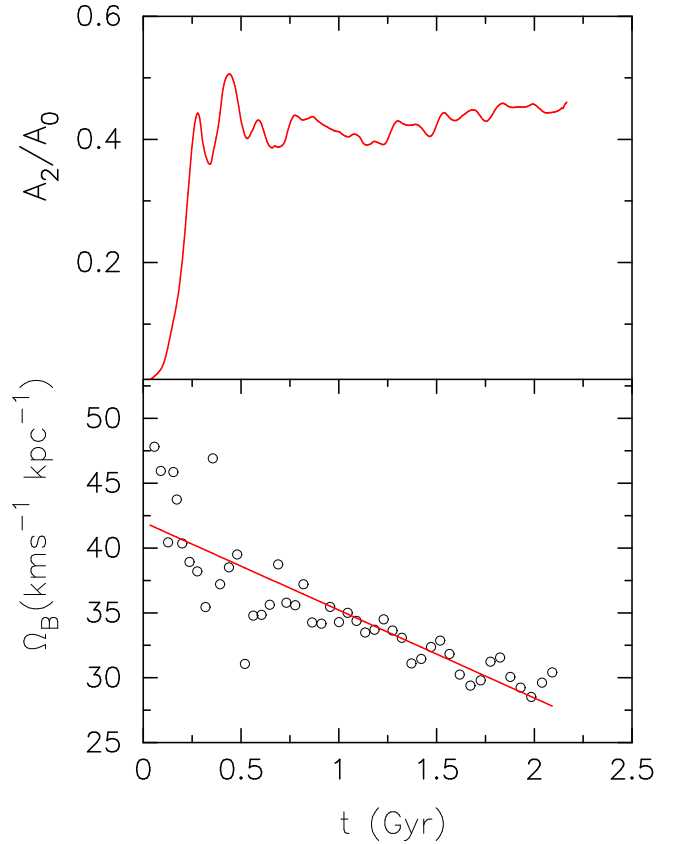


**Figure 3.** Time evolution of the bar amplitude and the pattern speed ( $\Omega_B$ ). Red solid line is the result of a linear regression analysis done on the measured pattern speed values from the  $N$ -body snapshots.

not real. Such a ring-like feature arises because of the galaxy model not being in perfect equilibrium.

In the upper panel of Fig. 3, we show the time evolution of the bar amplitude measured as the maximum of  $m = 2$  Fourier coefficient ( $A_2$ ) of the density perturbation normalized to the unperturbed axisymmetric component ( $A_0$ ). The bar reaches its first peak in amplitude at 0.28 Gyr and the second peak at 0.44 Gyr. The  $m = 1$  vertical Fourier mode ( $|A_{1,z}|$ ) in the  $r - z$  plane corotating with the bar pattern speed shows that the disk is undergoing buckling instability from  $\sim 0.39 - 0.6$  Gyr and strong buckling occurs around 0.6 Gyr.

Based on the nature of the growth curve, bars are classified into two broad categories, type-I and type-II. Type-I bars are strong, grow within a few orbital time scales and nearly saturate in amplitude, whereas type-II bars are weak, the growth time scale is very long (typically, a secular evolution time scale) and show no sign of saturation (Saha et al. 2010). The bar in our model is a type-I bar (e.g., Fig. 3).

The bottom panel of Fig. 3 shows the evolution of the bar pattern speed. The pattern speed of the bar decreases over time in our simulation, primarily because of the dynamical friction (Tremaine & Weinberg 1984; Weinberg 1985) against the dark matter halo. A detailed account on the bar's pattern speed decrease and its dependence on various dark matter halo properties e.g. halo angular momentum, orbital anisotropy, central concentration can be found



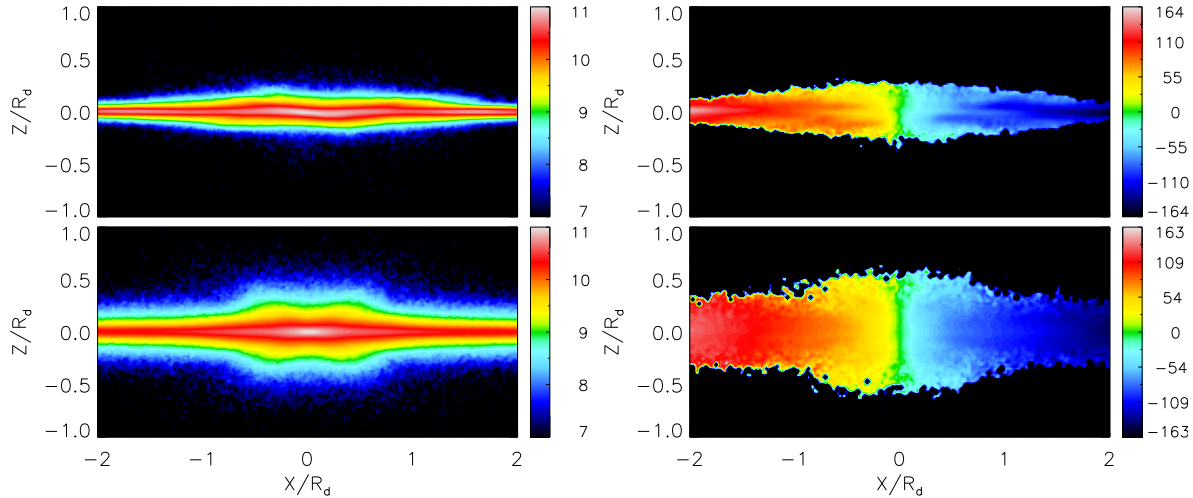


**Figure 4.** Edge-on surface density (left) and velocity maps (right) for the disk particles alone at two different epochs during the secular evolution. From top to bottom, the panels are taken at  $T = 0.56$  and 2.1 Gyr.

in Debattista & Sellwood (2000). Using a linear regression analysis on the simulation data, we find the half-life,  $T_{1/2}$ , (the time period over which the bar pattern speed would decay to half its initial value) of the rotating bar to be  $\sim 3.09$  Gyr. This indicates that the rate of angular momentum transfer from the bar is rather slow in our simulation; for an in-depth analysis on the bar slow down, readers are referred to Weinberg (1985); Weinberg & Katz (2007a).

As the bar grows stronger, its self-gravity increases and it goes through the well-known buckling instability (Combes & Sanders 1981; Pfenniger & Norman 1990; Raha et al. 1991; Martinez-Valpuesta & Shlosman 2004) following which the bar transforms into a boxy/peanut bulge. In Fig. 4, we present the surface density (left panels) and velocity field (right panels) for the boxy bulge seen edge-on; i.e., only disk particles are shown. The cylindrical rotation is evident. The final boxy bulge contains approximately 33% of the disk mass including the inner barred disk component. Note that the density drops off sharply along the vertical direction in the boxy bulge region. In Section 6, we will compare the structure and kinematics of the boxy bulge in Fig. 4 formed in our simulation with the classical bulge undergoing the bar driven secular evolution.

## 5 ANGULAR MOMENTUM TRANSFER TO THE CLASSICAL BULGE

We compute the specific angular momentum for each species e.g., disk, bulge and halo particles in our simulation and re-confirm the already established fact that the inner regions of the disk lose angular momentum through the bar. While a significant fraction of the total angular momentum emitted by the bar is absorbed by the surrounding dark matter halo, the angular momentum gained by the bulge is non-negligible. In Fig. 5, we show the angular momentum transfer amongst the disk, bulge and halo components in our model. The total angular momentum is conserved within 3% at the end of 2.2 Gyr in our simulation. Initially both the bulge and halo have zero net angular momentum i.e., they start as non-rotating objects. Note that the rate of gain of

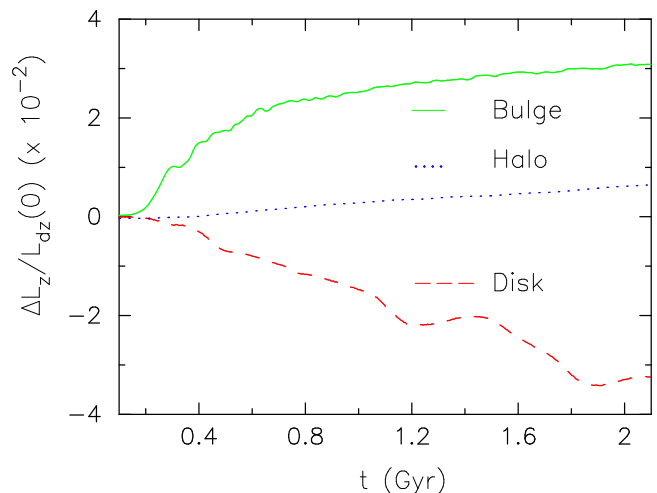


**Figure 5.** Evolution of the specific angular momentum of the bulge (green), disk (red) and halo (blue) components in our model. Along the y-axis plotted are the specific angular momentum minus its value at  $T = 0$  normalized by the disk angular momentum ( $L_{dz}(0)$ ) at  $T = 0$ .

angular momentum by the classical bulge particles nearly saturates towards the end of the simulation and closely follows the growth of the bar (see Fig. 3). Using orbital spectral analysis, we show below that the gain of angular momentum by the bulge occurs primarily through resonances (see also Hernquist & Weinberg 1992).

The simulation presented here shows an increase in the bulge rotation velocity (Section 6.2), and a corresponding increase in bulge angular momentum. The transfer of angular momentum from the bar to the bulge depends strongly on the pattern speed which sets the resonance locations. It is important to note that if the resonances are sparsely populated because of lack of particles in the simulation, the angular momentum transfer will be inefficient (Weinberg 1985; Weinberg & Katz 2007b). In our case, we have a total of  $10^7$  particles with  $10^6$  particles in the classical bulge. So we can test whether angular momentum transfer through reso-

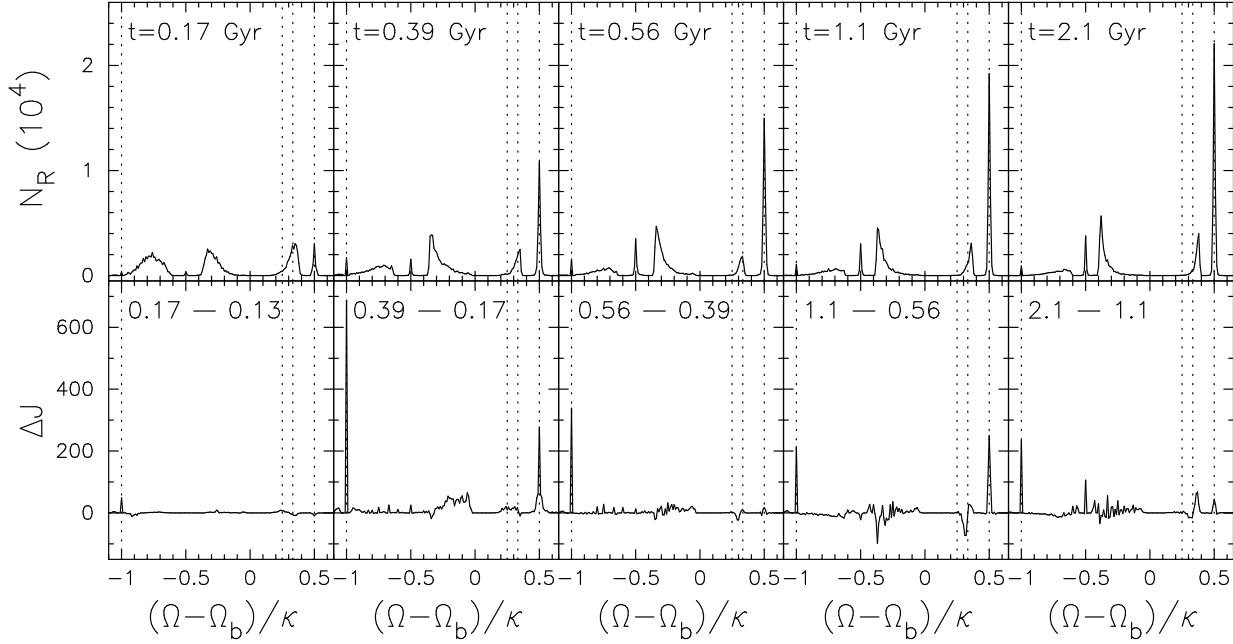


**Figure 6.** The top panels show the distribution of particles with frequency  $(\Omega - \Omega_b)/\kappa$  at five different times throughout the evolution of the bulge. The lower panels show the gain of angular momentum of the selected particles with respect to the previous time, as indicated on the top of the panel. The vertical dotted lines in the figure indicate the most important resonances, -1:1, 2:1, 3:1 and 4:1. Note that from time 1.1 Gyr to 2.1 Gyr the particles trapped at around  $(\Omega - \Omega_b)/\kappa = 0.5$  gain less angular momentum than earlier.

nant interaction, is the mechanism for the angular momentum gain of the classical bulge. Here, we quantify its effect by using an orbital spectral analysis method described in Martinez-Valpuesta et al. (2006) based on that presented in Binney & Spergel (1982). In previous works, this method was applied to halo resonant orbits (Athanasoula 2003; Martinez-Valpuesta et al. 2006; Dubinski et al. 2009) to understand the bar-halo interaction. We apply it to the classical bulge particles to find out how many of them are trapped in resonances and what is the corresponding gain of angular momentum. The potential is extracted from the  $N$ -body simulation at different snapshots using the grid code provided by Sellwood & Valluri (1997) and then frozen to compute the orbits. We randomly select 100000 (10%) particles out of 1 million in the bulge and compute their corresponding orbits. We calculate the azimuthal and radial epicyclic frequencies  $\Omega$  and  $\kappa$  respectively for each of the orbits by Fourier analysis.

We present the results of this orbital spectral analysis in Fig. 6 at 5 different epochs. On the top panels, we present the classification of classical bulge particles by their frequency ratio  $\eta = (\Omega - \Omega_b)/\kappa$ . The bar has an irregular evolution and this can be seen in the time sequence of the top panel in Fig. 6. Initially, the bulge particles are distributed half co-rotating with the disk and half counter-rotating. Therefore, when we study the orbital distribution in the very early stage of the bar growth at  $T = 0.17$  Gyr, there still is an almost symmetric distribution. When the bar is already formed, right after reaching the maximum, at  $T = 0.39$  Gyr, many particles have been trapped around the 2:1 resonance. Taking a careful look at these orbits, we have checked that they are of x1-type. There is also a considerable group of particles with  $\eta \in (-0.4, 0.)$ ; a look to the orbits allows to identify them as mainly stochastic trajectories. In the lower panels,

we show the angular momentum gain by the particles at each  $\eta$  during the growth and evolution of the bar. There is a considerable gain of angular momentum by three main groups in our diagram (Fig. 6, second bottom panel). The main gain of angular momentum comes from those particles at resonance with  $\eta = -1$ , corresponding to particles orbiting around the Lagrangian points. Since these particles are at negative frequency it means that they are counter-rotating with the bar. Another gaining group corresponds to the particles with  $\eta \in (-0.4, 0.)$ , the stochastic group. By gaining angular momentum their (counter) rotation decreases. Amongst the low order resonances, the important gaining group is around the ILR ( $\eta = 0.5$ ). We can conclude that at this stage of evolution, which is very rapid, the main transfer of angular momentum occurs through resonant and stochastic orbits.

During the period of evolution between  $T = 0.56 - 0.39$  Gyr, the bar goes through the buckling event, therefore there is still some trapping of particles around the 2:1 resonance. Although there not much gain or loss of angular momentum, some angular momenta are gained through  $\eta = -1$  resonance during this period. Notice that in the upper row of panels, the number of bulge particles trapped at the bar's ILR (2:1) is increasing. In the forth panel, at  $T = 1.1$  Gyr, we have 36% of particles trapped around the 2:1 resonance. At this time, the main gain of angular momentum comes from resonances at the ILR ( $\eta = 0.5$ ), and at  $\eta = -1, -2$ . The particles at the OLR ( $\eta = -0.5$ ) and those with  $\eta \in (-0.4, 0.)$  are losing angular momentum. At  $T = 2.1$  Gyr the classical bulge is still gaining angular momentum through resonances at ILR and  $\eta = -1$  corresponding to the Lagrange points. Note that some of the angular momentum gain is also coming from the OLR. Although the number of particles trapped at the ILR is gradually increas-

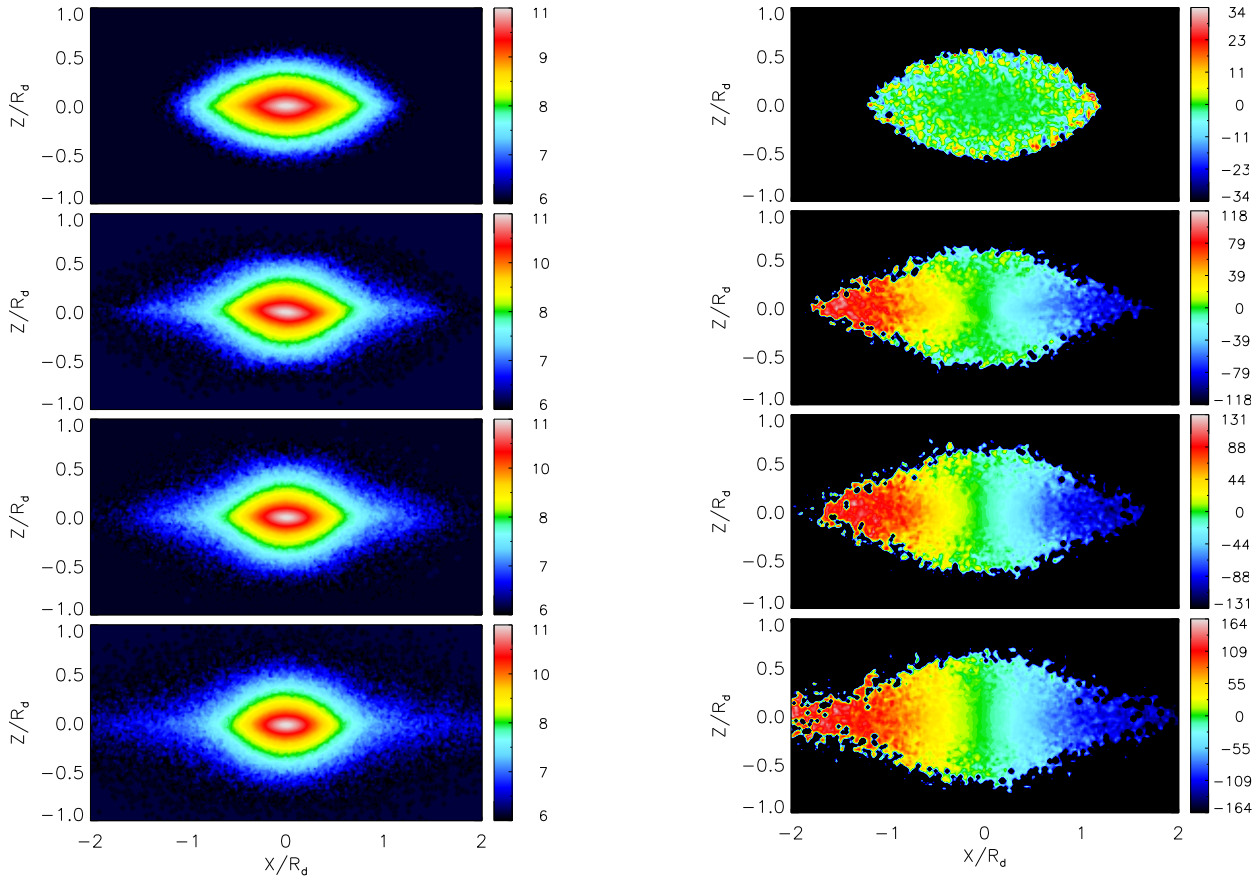


**Figure 7.** Edge-on surface density and velocity maps for the bulge particles alone at four different epochs during the secular evolution. From top to bottom, the panels are taken at  $T=0, 0.56, 1.1$  and  $2.1$  Gyr. The left panels show the surface densities and the right panels the velocity fields. Initially the bulge is non-rotating and flattened by the disk potential. Similar maps for the boxy-bulge are shown in Fig. 4.

ing over time, their angular momentum gain does not follow accordingly. By comparing the last two panels (upper and lower), it is evident that the particles trapped at the ILR are now hardly gaining angular momentum. It is plausible that the inner bar-like structure in the classical bulge (see section 6.3) is giving away angular momentum to the outer parts of bulge and perhaps to disk and halo.

The gain of angular momentum by the bulge can thus be explained by resonances during the slow secular evolution of the bar, and by resonances together with stochastic orbits in the dynamical stage. During the dynamical phase,  $T = 0.56 - 0.17$  Gyr, the net gain of angular momentum (computed by adding up the averaged angular momentum of each orbit) is 3 times larger than that gained in the relatively quiet secular phase ( $T = 2.1 - 0.56$  Gyr). While approximately 70% of the net angular momentum gain comes from the resonances, stochastic orbits contribute to  $\sim 30\%$  of the net angular momentum gained during the dynamical phase.

Previous studies of angular momentum transfer to the live dark matter halo (e.g., Athanassoula (2003); Martinez-Valpuesta et al. (2006); Dubinski et al. (2009)) have found important contribution from corotation, outer Lindblad resonance (OLR) and higher order resonances. By contrast, in the case of a small classical bulge as studied here, the OLR and corotation have not played any significant role

in the gain of angular momentum as shown above. This is most probably due to the fact that the size of the bulge in our simulation is much smaller than the typical size of the dark matter halo; the bulge half-mass radius ( $R_{1/2}^b = 0.21R_d$  and  $0.225R_d$  at  $T = 1.1$  and  $2.1$  Gyr respectively) is shorter than the bar size ( $R_{bar} = 0.987R_d$  and  $2.01R_d$  at those times) in our simulation. The bar size is measured from the phase angle of the bar (Athanassoula & Misiriotis 2002). The phase angle of the bar (i.e., the  $m = 2$  Fourier component of the disk surface density) remains approximately constant up to a certain radius and starts varying beyond that. We measure the length of the bar as the radius at which the phase angle of the bar starts deviating from the constant value. We also note that the corotation resonance ( $R_{cr} = 0.994, 1.12$  and  $1.30R_d$  at  $T = 0.56, 1.1$  and  $2.1$  Gyr respectively) of the bar is clearly outside the radius confining most of the bulge particles. The ratio of  $R_{cr}/R_{bar}$  lies between  $1 - 1.4$  at times mentioned in Fig. 6. As shown in Fig. 6, more and more particles in the classical bulge are trapped at the bar's ILR as time progresses. During the slow secular evolution, we can affirm that the mechanism acting in our system is the transfer of angular momentum through resonances. On the other hand, during the rapid dynamical evolution, resonant as well as stochastic orbits played an important role in transferring a significant fraction of the net angular momentum to the classical bulge. This angular momentum transfer

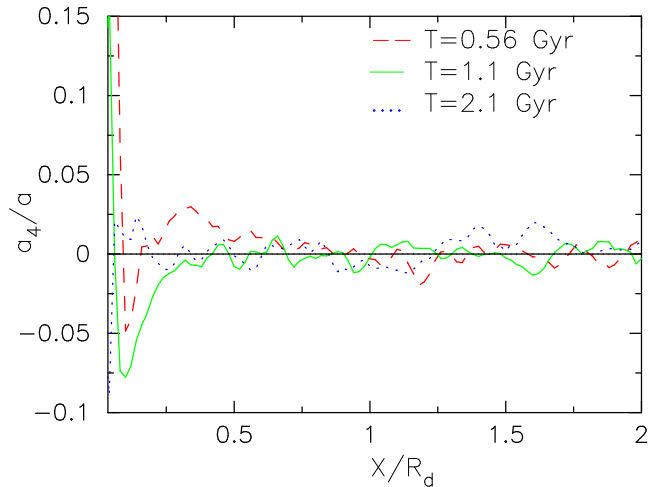


**Figure 8.** Normalized radial profile for the  $a_4$  coefficient for the classical bulge alone at three different times.

and the subsequent change of the orbital structure of the classical bulge are indeed responsible for the transformation of the classical bulge as described below.

## 6 EVOLUTION OF THE CLASSICAL BULGE - STRUCTURE AND KINEMATICS

From Sections 2 and 5, we learn that a classical bulge can absorb a non-negligible fraction of the total angular momentum emitted by the bar through resonant interaction. The angular momentum gained by the bulge (being a smaller mass object than the dark matter halo) has a profound effect on its structure, kinematics and dynamics. The result of the bar-bulge interaction in our simulation is the *transformation of an initially non-rotating low mass classical bulge into a highly rotating triaxial one*. Below we describe, in considerable detail, various diagnostics which show that this is indeed true.

### 6.1 Surface brightness

In the left panels of Fig. 7, we show the surface density maps for the classical bulge (viewed edge-on) at four different epochs during the evolution. The classical bulge is shown edge-on ( $i = 90^\circ$ ) such that the major axis is along  $X$ -axis and the minor axis along  $Z$ -axis. Initially the bulge is isotropic and flattened by the strong gravity of the disk potential. At later phases of evolution, the inner regions of the bulge become rounder and the outer parts become disk.

In order to understand the structure of the classical bulge more quantitatively, we have also performed an isophotal analysis using the IRAF ellipse task on a set of edge-on images of the bulge including the ones presented in Fig. 7, and compute the fourth-order Fourier cosine coefficient  $a_4/a$  normalized to the semi-major axis  $a$  at which the ellipse was fit. Fig. 8 shows the normalized  $a_4$  profiles at three different epochs in the simulation. The values of  $a_4/a$  determine the degree of boxiness or diskiness (Nieto & Bender 1989), with  $a_4/a < 0$  denoting a boxy isophote,  $a_4/a > 0$  a disk isophote, and  $a_4/a \sim 0$  means elliptical or round isophote. The inner region ( $X/R_d \leq 0.2$ )

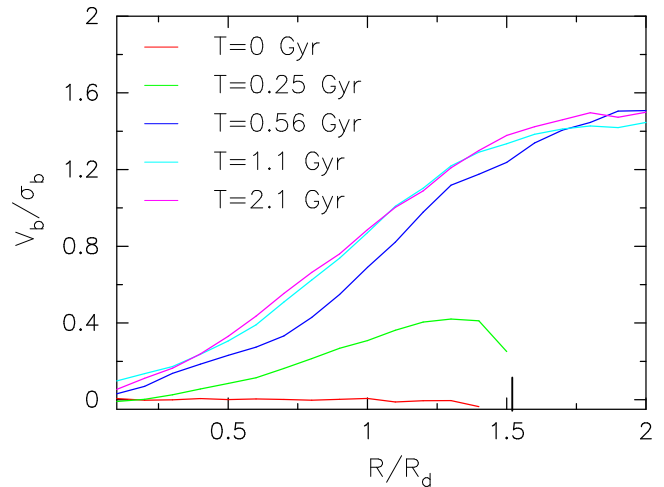


**Figure 9.** Radial variation of the bulge rotational velocity normalized to the average velocity dispersion in the central region, for five snapshots from  $T=0$  to  $T=2.1$  Gyr. The long tick mark on the x-axis denotes the initial value of  $R_b$ , see Table 1.

of the classical bulge becomes mildly boxy at  $T = 0.56$  Gyr and the boxiness increases at 1.1 Gyr as can be seen from Fig. 8 and Fig. 7. On the other hand, at  $T = 2.1$  Gyr,  $a_4/a > 0$  in the outer parts of the bulge indicating disk isophotes. Recall that the disk has a boxy bulge formed as a result of the bar buckling instability as shown in Fig. 4. In order to compare properties of the classical bulge and boxy bulge, we have measured the  $a_4/a$  parameter of the boxy bulge in a similar fashion as outlined above. It is found that at  $T = 1.1$  Gyr,  $a_4/a$  of the boxy bulge is negative inside  $X/R_d < 1.0$  and its maximum value is about twice that of the classical bulge. From the minor axis density profiles calculated separately for the classical bulge and the boxy bulge region, we find that initially the classical bulge extends further above the disk midplane, and its central surface density is 2.4 times lower than that of the disk. As the disk goes through the buckling instability, the particles settle into the 3D boxy bulge. We find that at  $T = 1.1$  Gyr the boxy bulge is more concentrated toward the disk midplane ( $z = 0$ ) and its midplane surface density is  $\sim 3$  times higher than that of the classical bulge. At this time, the density of classical bulge above  $z = 0.17R_d$  is higher than that of the boxy bulge, and the classical bulge extends further. However, at  $T = 2.1$  Gyr, the boxy bulge dominates over the classical bulge for  $z \leq 0.39R_d$  and above this height, their density profiles are comparable.

### 6.2 Rotational properties

The influx of angular momentum to the initially non-rotating bulge enforces the bulge particles to have a net rotational motion. In Fig. 9, we show the radial profiles of the rotational velocity normalized to the average velocity dispersion in the central region ( $R \leq R_{1/2}^b$ ) of the classical bulge at different epochs during the evolution. The rotational velocity profiles remain nearly unchanged at later stages of evolution when the rate of angular momentum gain by the bulge also nearly saturates as can be seen from Fig. 5 and Fig. 6.



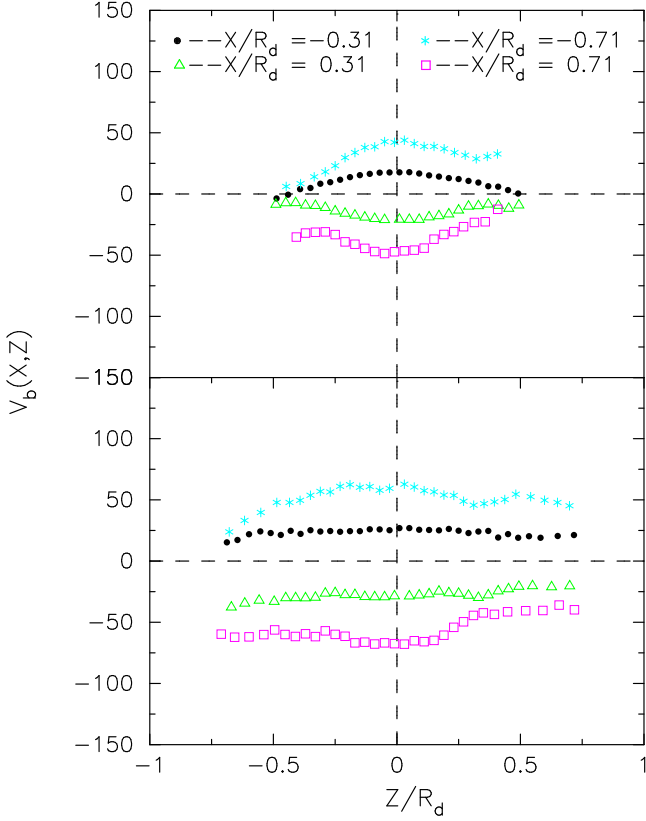


**Figure 10.** Parallel minor axis velocity profiles of the bulge at  $T=0.56$  Gyr (upper panel) and  $T=2.1$  Gyr (lower panel). The upper panel shows no clear signature of cylindrical rotation. But at later stages of the evolution, cylindrical rotation develops in the inner region of the bulge, as indicated by the parallel shapes of the velocity profiles in the lower panel.

To illustrate the evolution further, we present four velocity maps of the classical bulge on the right panels of Fig. 7. During the initial phases of secular evolution, the angular momentum gained by the bulge particles is primarily converted into streaming motion and the classical bulge starts rotating around the  $z$ -axis, with gradients in the streaming velocity both along the radial and vertical directions. Note that in the barred potential, the classical bulge is no longer axisymmetric and its inner regions becomes moderately boxy (see Sections 6.1 and 6.3). This could be a signature of a thick bar formed inside the classical bulge (see Section 6.3). Indeed as time progresses, mild signatures of cylindrical rotation emerge in the inner regions of the bulge and gradually become prominent (see Fig. 7).

To have a clearer picture of the velocity structure, we show parallel minor-axis (Fig. 10) and major-axis (Fig. 11) velocity profiles of the classical bulge at two different epochs  $T = 0.56$  (upper panels) and  $T = 2.1$  Gyr (bottom panels). The minor-axis velocity profiles are drawn at two different radii ( $X/R_d = 0.31$  and  $X/R_d = 0.71$ ) on either side of the bulge center. At  $T = 0.56$  Gyr, the minor axis rotation velocity decreases along the vertical direction ( $\frac{dV_b}{dz} < 0$ ) indicating clearly a non-cylindrical rotation throughout the bulge (see the upper panel of Fig. 10). Note, the velocity profiles in the outer parts are asymmetric which is probably influenced by the on-going buckling instability of the bar.

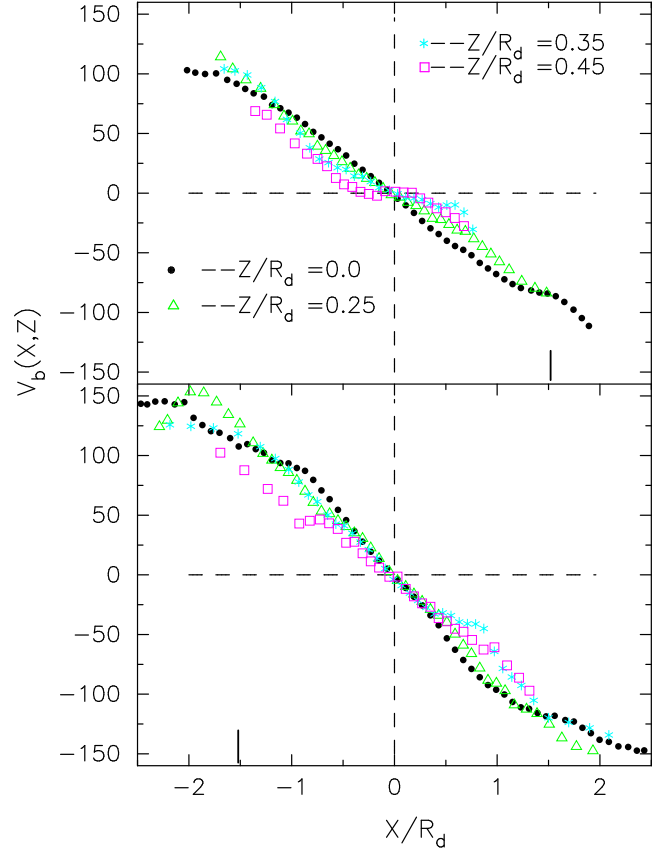


**Figure 11.** Major axis velocity profiles of the bulge at  $T=0.56$  Gyr (upper panel) and  $T=2.1$  Gyr (lower panel). The upper panel shows no clear signature of cylindrical rotation. But at later stages of the evolution, cylindrical rotation develops in the inner region of the bulge. The long tick mark on the x-axis denotes the initial value of  $R_b$ , see Table 1.

The major-axis profiles are taken at four different slits (the slit positions are indicated in Fig. 11) parallel to the major axis of the classical bulge. The major-axis velocity profiles in the upper panel of Fig. 11, also indicate non-cylindrical rotation throughout the classical bulge.

At later times, the inner regions of the classical bulge have developed cylindrical rotation. However, the gradient of this cylindrical rotation in the classical bulge is shallower than that in the boxy bulge. The minor-axis velocity profiles in the bottom panel of Fig. 10, show clear indication for that in the inner regions. The same is evident from the bottom panel of Fig. 11. The major axis velocity profiles at  $T = 2.1$  Gyr clearly demonstrate that the inner regions ( $X/R_d < 0.4$ ) of the classical bulge rotate cylindrically while the outer regions beyond about twice the half-mass radius ( $2 \times R_{1/2}^b \sim 0.45R_d$ ) still maintain differential rotation both along the radial and vertical directions ( $\frac{dV_b}{dz} < 0$ ). *So in the later stages of the secular evolution, the initially non-rotating classical bulge has developed a mixed rotational state with the inner region rotating cylindrically while the outer region rotates differentially in  $z$ .*

### 6.3 The classical bulge-bar

In order to achieve a deeper understanding of the complex non-linear dynamical interplay of the bar and the bulge, we investigate the three dimensional structure of the classical bulge using spherical harmonics analysis. In particular, we are looking for non-axisymmetric modes in the classical bulge which could have been influential for producing some of the complex structure and kinematics as discussed in Sections 6.1 and 6.2. The outcome of the bar-bulge interaction is not only the transfer of angular momentum between the two and changes in kinematics thereby, but a structural transformation of the classical bulge, a prediction of which is probably beyond the scope of the analytic/semi-analytic theories (Lynden-Bell & Kalnajs 1972; Tremaine & Weinberg 1984) briefly outlined in Section 2. From our analysis, it becomes clear that the interaction of a bar and a small classical bulge is more vigorous than that between the bar and the massive dark halo as discussed in section 2. The primary reason being the smaller mass and size of the bulge compared to the dark matter halo.

To analyze the structural components developed in the small classical bulge after the evolution, we expand the full three dimensional bulge density distribution ( $\rho$ ) in terms of spherical harmonics:

$$\rho(r, \theta, \phi) = \sum_{l=0}^{\infty} \sum_{m=-l}^l \rho_{lm}(r) Y_l^m(\theta, \phi), \quad (5)$$

where  $r, \theta, \phi$  are the usual spherical coordinates, and the  $Y_l^m$  are the spherical harmonics.  $\rho_{lm}$  denotes the radial density function. We bin the bulge particles into spherical shells and compute  $B_{lm}$  as function of the bin radius ( $r_k$ ), as follows:

$$B_{lm}(r_k) = N_{lm} \sum_j m_b P_l^m(\cos \theta_j) e^{im\phi_j}, \quad (6)$$

where  $N_{lm} = ((2l+1)/2\pi) \times (l-m)!/(l+m)!$ ,  $m_b$  is the mass of each bulge particle,  $P_l^m$  are the Associated Legendre polynomials. The function  $B_{lm}$  is directly related to the mass of each bin and thereby to  $\rho_{lm}$  via the bin radius ( $r_k$ ). Then using the above formula (Eq. 6), we can derive the radial variation of the amplitude of a particular  $l, m$  mode in the bulge as  $S_{lm}(r_k) = \sqrt{\Re B_{lm}^2 + \Im B_{lm}^2}$ . The corresponding phase angle  $\phi_j$  can be used to derive the pattern speed of the  $l, m$  mode.

In Fig. 12, we show the time evolution of the amplitude of  $l = 2, m = 2$  mode. The classical bulge-bar (hereafter, denoted as ClBb) is weaker than the disk bar (see Fig. 3 for the bar amplitude and pattern speed) but rotates nearly in phase with it. By analyzing the radial variation of the phase angles, we conclude that the physical size of the ClBb is much smaller compared to the disk bar. Initially, the ClBb and disk bar are not in phase, the ClBb seems to be lagging behind the disk bar by about  $2^\circ - 4^\circ$  in angle. But soon, they start rotating in-phase with each other. After about 1 Gyr, the pattern speed of the ClBb is also nearly the same as that of the disk bar (see Fig. 12). A convenient way of viewing the dynamics of the ClBb, is to think of it initially as a driven oscillation phenomenon where the disk bar is acting as a driver and the bar-like structure in the classical bulge is its forced response. Later bulge particles are trapped by the 2:1 resonance; i.e., both components populate the or-

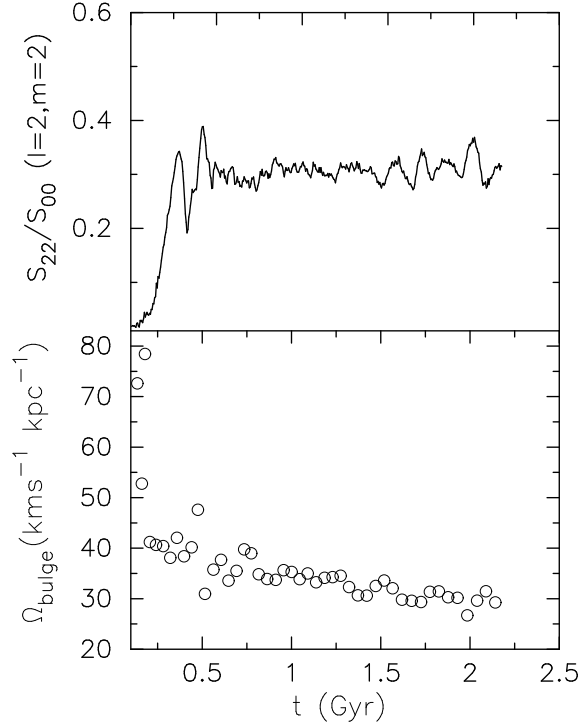


**Figure 12.** The strength of the classical bulge-bar ( $l=2, m=2$  mode) and its pattern speed evolution.

bits in their jointly rotating potential. It has been shown in previous simulations e.g., by Holley-Bockelmann et al. (2005), Colín et al. (2006), Athanassoula (2007) that a bar-like structure also forms in the inner regions of the dark matter halo as a result of its interaction with the bar in the disk. These studies have shown that such a bar in the halo is rather weak and nearly corotates with the bar in the disk. It turns out that some of the characteristics of the ClBb are quite similar to that of the halo-bar. However, with the classical bulge being much less massive than the halo, the dynamical impact of the bar-like structure is much more pronounced in the classical bulge as we have already demonstrated above. Beside the transfer of energy and angular momentum between the disk-bar and the classical bulge, the stars in the classical bulge are also being heated during the evolution and hence the inner bulge region becomes moderately thicker and rounder (see Fig. 7). We have checked that the slow variation in the ellipticity of the classical bulge is consistent with the variation in the kinetic energy tensor in accordance with the tensor virial theorem. A more detailed picture of the dynamics of the bulge hosting a bar and its observational properties will be presented in a future paper.

### 6.4 Triaxiality and anisotropy

From the misalignment of the photometric major axis of the disk and the bulge and the isophotal twists, it is inferred that many of the bulges in spiral galaxies are indeed triaxial (Stark 1977; Gerhard et al. 1989; Bertola et al. 1991; Ann 1995; Méndez-Abreu et al. 2010). Here, we show the evolution of the triaxiality and velocity anisotropy in the low mass classical bulge in our simulation. The global parameter for

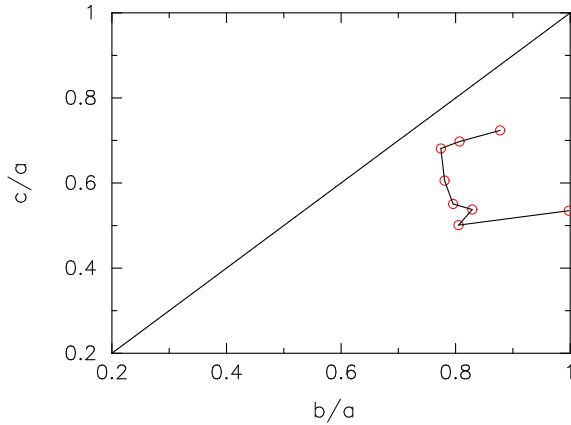


**Figure 13.** Time evolution of the shape of the classical bulge. Initially the bulge is flattened by the strong disk potential and hence oblate. At later phases during the secular evolution it becomes triaxial. The solid diagonal line denotes a prolate configuration. The red open circles are the measured values of the axes ratios at  $T = 0, 0.25, 0.393, 0.56, 1.1, 1.52, 1.77, 2.1$  Gyr.  $b/a = 0.99$  and  $0.877$  at  $T = 0$  and  $2.1$  Gyr respectively.

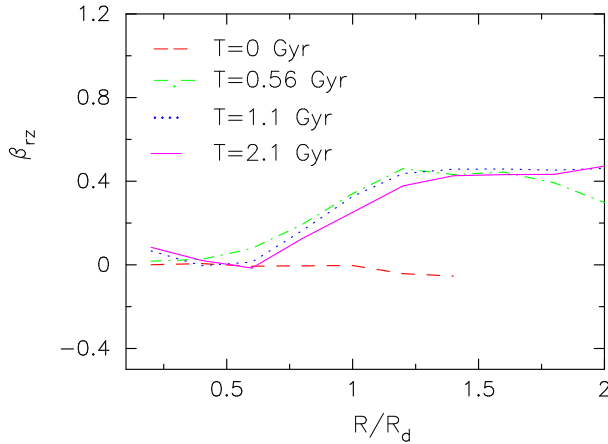


**Figure 14.** Radial variation of the anisotropy parameter  $\beta_{rz}$  for the classical bulge. Beyond about 0.56 Gyr, the anisotropy profiles remains nearly unchanged.

the bulge triaxiality  $T_b$  can be computed using the following relation (Franx et al. 1991; Jesseit et al. 2005):

$$T_b = \frac{1 - (b/a)^2}{1 - (c/a)^2}, \quad (7)$$

where  $a$ ,  $b$ , and  $c$  are the semi-axes defining the shape of the classical bulge (see Section 6.5 for the measurement of the axis ratios).  $a = b > c$  denotes an oblate configuration i.e.  $T_b = 0$ , and  $b = c < a$  is a prolate figure corresponding to  $T_b = 1$ .  $a \neq b \neq c$  defines a triaxial configuration with peak values reaching  $T_b = 0.5$ . In Fig. 13, we show the evolution of the shape of the classical bulge. Initially the bulge is oblate ( $T_b \sim 0$ , see Fig. 13); thereafter it evolves as a result of the angular momentum gain and change in the orbital structure. During the period of  $0.17 - 0.56$  Gyr (roughly the dynamical phase) a considerable fraction of angular momentum is gained at resonances  $\eta = -1$  corresponding to the Lagrange point orbits and  $\eta = 0.5$  (ILR) (see Fig. 6). This angular momentum gain cause the bulge particles to move outwards

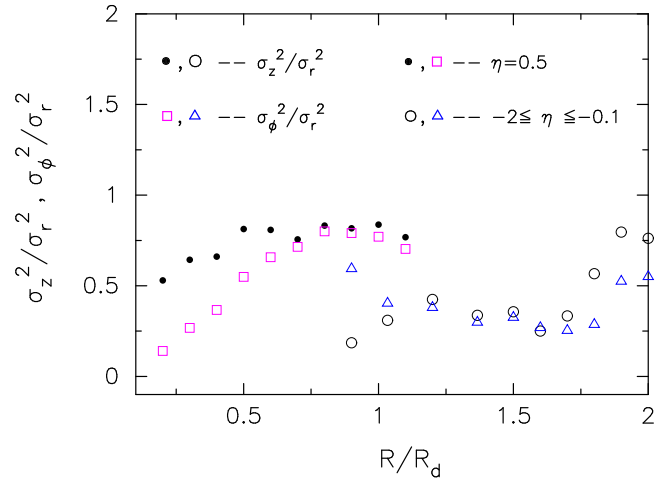


**Figure 15.** Radial variation of velocity dispersion ratios computed from bulge particles trapped at ILR ( $\eta = 0.5$ ) and from a group of resonant and non-resonant particles in the frequency range  $-2.0 \leq \eta \leq -0.1$  in the classical bulge. Orbits of these particles were computed at 1.1 Gyr.

and thereby producing a disky structure (see Fig. 7) in the outer parts of the bulge. In this period, essentially only  $b/a$  changes while  $c/a$  remains nearly constant.

Beyond  $\sim 0.56$  Gyr, the ClBb forms in the bulge causing substantial changes in the bulge structure. As mentioned in section 6.3, the ClBb heats (Saha et al. 2010) the bulge stars mainly in the central region and makes it thicker. We think that this heating due to ClBb is primarily responsible for subsequent changes in the  $c/a$ . During the period from 1.5–2.1 Gyr,  $b/a$  changes more than  $c/a$ . At  $T = 2.1$  Gyr, the small classical bulge is triaxial with  $T_b = 0.48$ . This suggests that more generally, fast rotating and triaxial bulges could have developed through the interaction of a strong bar and a small classical bulge in galaxies with low  $B/D$  ratio. A more comprehensive analysis focusing on the role of the most important parameters such as the bulge mass and size will be presented in a future paper.

As shown in Section 3, the initial velocity distribution in the classical bulge in our simulation is isotropic represented by a King model. As a result of the angular momentum influx and the readjustment of the orbits, the velocity structure changes during the evolution. We measure the deviation from isotropy in the velocity distribution by the anisotropy parameters defined as  $\beta_{rz} = 1 - (\sigma_z/\sigma_r)^2$  and  $\beta_{r\phi} = 1 - (\sigma_\phi/\sigma_r)^2$ , where  $\sigma_r$ ,  $\sigma_\phi$  and  $\sigma_z$  are the velocity dispersions in the radial, azimuthal and vertical direction. Then  $\beta_{rz} > 0$  denotes radial anisotropy and  $\beta_{r\phi} < 0$  means tangential anisotropy. In Fig. 14, we show the profiles of the radial anisotropy at four different epochs calculated from all the particles in the classical bulge. We see that the classical bulge already becomes radially anisotropic at  $T = 0.56$  Gyr. To understand the source of radial anisotropy, we have studied orbits in the classical bulge as clarified in Fig. 6. Fig. 15 shows radial variation of  $\sigma_z^2/\sigma_r^2$  and  $\sigma_\phi^2/\sigma_r^2$  computed from bulge particles that are trapped at ILR ( $\eta = 0.5$ ) and from a group of resonant and non-resonant particles in the frequency range  $-2.0 \leq \eta \leq -0.1$  separately. The particles that are at ILR resonance (2:1) follow x1-type orbits and they produce the radial anisotropy in

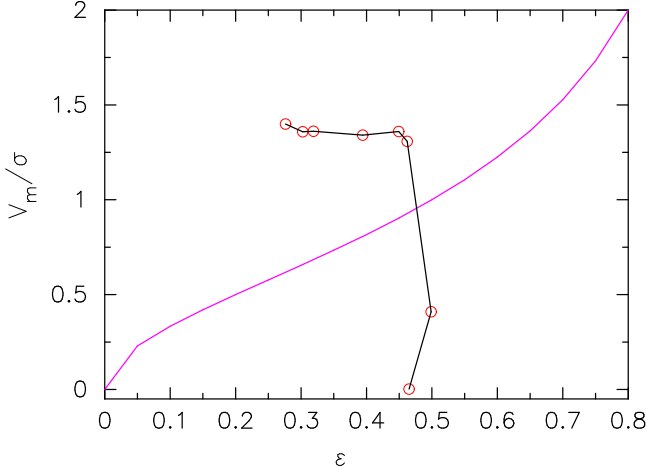


**Figure 16.**  $V_m/\sigma - \epsilon$  relation for the small classical bulge alone. Initially the bulge is non-rotating but then it acquires angular momentum emitted by the bar and evolves into a fast rotating triaxial bulge. Each open circle represents an epoch in the simulation beginning at  $T = 0$  (the bottom most point). Subsequent circles are drawn at 0.25, 0.393, 0.56, 1.1, 1.52, 1.77, 2.1 Gyr. The pink solid line is the reference isotropic rotator model.

the inner region of the classical bulge which host the ClBb. Whereas in the outer region, definite contributions to the radial anisotropy comes from the bulge particles in the frequency range  $-2.0 \leq \eta \leq -0.1$ . The particles that are at resonance with the bar e.g., at  $\eta = -2, -1$  follow regular orbits while the non-resonant particles are in stochastic orbits.

### 6.5 $V_m/\sigma - \epsilon$ relation

To quantify the degree of ordered motion in bulges and ellipticals and illuminate the difference between the two types of stellar systems, the  $V_m/\sigma - \epsilon$  diagram relating the ratio of rotational to random motions and the observed ellipticity ( $\epsilon$ ) was introduced (Illingworth 1977). It was shown that bulges are, in general, fast rotators compared to bright elliptical galaxies (Kormendy & Illingworth 1982; Davies et al. 1983; Cappellari et al. 2007; Morelli et al. 2008). Here, we focus on the relation between the shape and the kinematics of the simulated low mass classical bulge that has been subject to the secular evolution driven by a strong bar. We show explicitly the evolutionary track of this particular classical bulge in the  $V_m/\sigma - \epsilon$  diagram below (Fig. 16).

In observations, it is rather difficult to have an accurate measurement of the bulge rotation velocity due to possible disk contamination. On the other hand, in simulations, it is rather straightforward to compute the velocity profile for the classical bulge alone because it is possible to filter out the disk and halo components of the model galaxy. We determine,  $V_m$  as the maximum of the azimuthally averaged rotational velocity of the bulge particles measured in the equatorial plane of the bulge;  $\sigma$  is the mean velocity dispersion in the central region (calculated at  $r \sim 0.5 \times R_{1/2}$ ) of the bulge.

For the bulge ellipticity, we use  $c/a$  for edge-on view. Measuring the ellipticity for a bulge is a bit tricky because there can be strong radial variation in the ellipticity pro-

file  $\epsilon(r)$ . Triaxiality could add another degree of complexity to such a measurement. Below we describe how the bulge ellipticities are measured.

In order to determine the intrinsic ellipticity, we first compute the moment-of-inertia tensor of the three dimensional mass distribution of the classical bulge and diagonalize it to obtain the principal moments and three orthogonal eigenvectors. The principal moments of inertia determine the intrinsic axis ratios of the inertia ellipsoid and the eigenvectors determine the orientation of the ellipsoid with respect to the co-ordinate space. Using the eigenvalues and eigenvectors, we determine the two axis ratios namely  $b/a$  and  $c/a$ , where  $a > b > c$  are the three semi-axes of the inertia ellipsoid. We have done this at the bulge half-mass radius containing 50% of the total bulge particles and at the radius containing about 90% of the total bulge particles. The ellipticity measurements for the classical bulge are nearly the same in both cases. In the following, we use the ellipticity at radii enclosing  $\sim 90\%$  of the total bulge particles and use the definition of the ellipticity of the bulge as  $\epsilon = 1 - c/a$  when viewed edge-on. We have also performed isophote analysis using the ellipse-fitting routine from IRAF on a set of suitably rotated and inclined edge-on images (Fig. 7) of the classical bulge at different epochs during the evolution. We find a good agreement between the two different types of measurements of the bulge ellipticity.

In Fig. 16, we show the  $V_m/\sigma$  and  $\epsilon$  values for the small classical bulge during the secular evolution. Each point in this diagram corresponds to a particular epoch during its evolution and when connected together they form its evolutionary track. This shows that the small classical bulge rotates significantly faster in the latter stages of evolution compared to the oblate isotropic rotator model, which can be approximated by (Binney 1978; Kormendy 1982):

$$V_m/\sigma \cong \sqrt{\frac{\epsilon}{1-\epsilon}}. \quad (8)$$

The interpretation of Fig. 16 is complicated by the fact that the classical bulge is not an isolated stellar system, but interacts dynamically with the bar within a disk galaxy. The entire period of evolution of the classical bulge can be broadly divided into two parts: one before the formation of the ClBb ( $\sim 0.56$  Gyr) and the second after its formation. Before the formation of the ClBb, the bulge stars in the outer region gain a significant fraction of angular momentum emitted by the bar and move mainly outwards in radius. As a result of this, the values of  $V_m/\sigma$  increase till  $\sim 0.56$  Gyr while the axis ratio  $c/a$  remains unchanged. In the second half of the evolution, the bulge stars are heated due to the ClBb by a factor of  $\sim 1.5$  in velocity dispersion and this makes the inner region rounder. So  $c/a$  ratio increases, making the ellipticity decrease considerably. The near saturation in the  $V_m/\sigma$  towards the end of the simulation is connected with the fact that the rate of angular momentum gain by the bulge nearly saturates at these epochs (see Fig. 5, Fig. 6). A more detailed analysis on how the spinning up of the classical bulge depends on the various parameters of the bulge (bulge-to-disk mass ratio, size of the bulge, its central velocity dispersion) and disk (Toomre Q, bar strength, bar size) will be presented in a future paper.



## 7 DISCUSSION

The primary goal of this paper has been to describe a generic mechanism, the transfer of angular momentum from a bar to an embedded classical bulge. We have shown that this mechanism is important for understanding the rotational motion of low mass classical bulges in the central regions of barred galaxies. The growth rate and the strength of the bar are important factors for the mechanism to work efficiently. One very interesting outcome of this process is the cylindrical rotation in the small classical bulge in the model studied here. Some possible observational implications and other issues are addressed below.

### 7.1 Structural impact on the bulge

During the secular evolution, a flat bar transforms into a boxy bulge. While the bar grows, buckles and evolves, a fraction of the angular momentum emitted by the bar is absorbed mainly in the outer parts of the embedded classical bulge in the galaxy. As a result, streaming motions are induced in the classical bulge (Fig. 9), and the orbital structure changes, causing velocity anisotropies. After about half a Gyr, the ClBb forms in the inner regions of the bulge. The ClBb introduces a pattern rotation in the classical bulge which transforms into a rotating triaxial object. A comparison of Fig. 3 and Fig. 12 shows that beyond  $\sim 0.8$  Gyr the ClBb essentially corotates with the boxy bulge formed out of the disk bar. Towards the end of the evolution, the model galaxy has a composite bulge: a superposition of the boxy bulge and a rotating triaxial classical bulge. At late times, the inner regions of the classical bulge become rounder as it is evident from the surface density maps (Fig. 7) for the classical bulge particles alone. We note that the stars in the classical bulge are heated by a factor of  $\sim 1.5$  in velocity dispersion within 2 Gyrs. The ClBb maybe responsible for heating the bulge stars in a similar fashion as the bar heats the disk stars (Saha et al. 2010).

### 7.2 Boxy bulge and net cylindrical rotation

It is widely accepted that cylindrical rotation is a characteristic feature of the kinematics of a boxy bulge formed out of disk material, via the vertical buckling instability of the bar. Thus the presence of cylindrical rotation in the central regions of a galaxy may lead one to infer the presence of a boxy bulge that originated from the disk, without any need for a classical bulge in this galaxy.

The work presented in this paper adds a new aspect to this simple picture. The cylindrical rotation could also include the stars of the classical bulge whose rotational properties have been modified by the interaction with the bar. One would measure the net cylindrical rotation of the stars in the combined boxy bulge and classical bulge. In absence of strong photometric evidence, other information such as from stellar populations and metallicity gradients would be needed to determine the presence of a small classical bulge.

Although the pure kinematic modelling of the BRAVA data (Shen et al. 2010) suggests only an upper limit on the mass of a classical bulge in the Milky Way, the measurements of the metallicity gradient above the galactic plane (Zoccali et al. 2008) may indicate the presence of a

classical bulge. The upper limit on the total mass of the bulge (boxy bulge + classical bulge) in our model, including the remaining disk component in the boxy bulge region, is  $\sim 1.46 \times 10^{10} M_\odot$ . Of this,  $0.29 \times 10^{10} M_\odot$  is in the classical bulge, and  $\sim 1.17 \times 10^{10} M_\odot$  in the boxy bulge and the central disk. Since the classical bulge extends further above the galactic plane than the boxy bulge, the metallicity composition of the composite system would change with height. We plan to investigate this further and use our model to look for signatures of the classical bulge from the metallicity distribution in order to compare with observations of the Milky Way.

### 7.3 Observing secular evolution through a classical bulge

Previous studies mainly based on  $N$ -body simulations have focused on the bar-halo interaction (Athanasoula 2002; Weinberg & Katz 2007a; Villa-Vargas et al. 2009; Dubinski et al. 2009) and shown that a significant amount of angular momentum emitted by the bar is absorbed in the dark matter halo. The angular momentum gained by the halo changes the internal structure of the dark matter halo. Some authors have utilized this mechanism of angular momentum exchange to resolve the cusp-core issue (El-Zant et al. 2001; Weinberg & Katz 2002; Sellwood 2008) in galaxies while others have focused on the halo-bar (Holley-Bockelmann et al. 2005; Colín et al. 2006; Athanasoula 2007). However, direct observational evidence for the halo-bar, and hence direct observational verification of the ongoing secular evolution and angular momentum transfer can not be obtained unless dark matter is detected. Unlike the dark matter, it is possible to observe galactic bulge stars in detail, both the kinematics and stellar population parameters. It is thus possible to verify observationally the bar-bulge interaction and the resulting dynamical properties of the ClBb. Observational evidence for the ClBb could be a direct confirmation of the angular momentum transfer and secular evolution in the galaxy.

## 8 CONCLUSIONS

The secular processes driven by the bar not only restructure the disk, but also the other components in the galaxy. Since the classical bulge is less massive here compared with the surrounding dark matter halo, the angular momentum gained by the classical bulge has a more significant effect on its evolution. The present work has shown in considerable detail that the unavoidable gravitational interaction between these two components can have profound implications for the structure of a low mass classical bulge, as highlighted below.

1. We have established that the main mechanism of angular momentum transport operating between the bar and the classical bulge is through resonances. The bulge particles gain angular momentum emitted by the bar through the bar's ILR ( $\eta = 0.5$ ), and other resonances with  $\eta = -1, -2$  and also through non-resonant orbits with  $\eta \in (-0.4, 0.)$  during the dynamical phase when bar growth is rapid. Approximately 3/4 of the net angular momentum is gained

by the classical bulge during the dynamical phase where stochastic orbits contribute  $\sim 30\%$ .

2. The angular momentum gained by the initially non-rotating classical bulge sets the bulge particles in rotational motion. The radial gradient in the rotational motion in the classical bulge is lower than in the boxy bulge. As time progresses the rotational velocity increases and nearly saturates at about 1 Gyr. At around this time, the inner regions of the classical bulge develop cylindrical rotation while the outer parts are still in differential rotation.

3. As a result of the angular momentum transfer, some of the bulge orbits are trapped by the rotating bar potential, a ClBb forms which essentially cororates with the bar, and the classical bulge transforms into a triaxial, anisotropic object where trapped orbits contributes to the radial anisotropy.

4. Towards the end of the secular evolution, the model galaxy has a composite bulge which is a superposition of the boxy bulge formed out of the disk material and the rotating triaxial, low mass classical bulge. The stars in the composite bulge rotates cylindrically. From an observational perspective, one would need other tracers such as metallicity gradient, stellar population parameters along with the kinematics to reliably determine the presence of such a low mass classical bulge embedded in the boxy bulge.

#### Acknowledgements

K.S. acknowledges support from the Alexander von Humboldt Foundation. It is a pleasure to thank Lodovico Coccato for his generous help with IRAF, Jerry Sellwood for letting us use his potential solver code, and Francoise Combes for valuable inputs. The authors thank the anonymous referee for useful comments.

#### REFERENCES

- Aguirri J. A. L., Balcells M., Peletier R. F., 2001, *A&A*, 367, 428
- Ann H. B., 1995, *Journal of Korean Astronomical Society*, 28, 209
- Athanassoula E., 2002, *ApJ*, 569, L83
- Athanassoula E., 2003, *MNRAS*, 341, 1179
- Athanassoula E., 2005, *MNRAS*, 358, 1477
- Athanassoula E., 2007, *MNRAS*, 377, 1569
- Athanassoula E., Misiriotis A., 2002, *MNRAS*, 330, 35
- Baugh C. M., Cole S., Frenk C. S., 1996, *MNRAS*, 283, 1361
- Bertola F., Vietri M., Zeilinger W. W., 1991, *ApJ*, 374, L13
- Binney J., 1978, *MNRAS*, 183, 501
- Binney J., Spergel D., 1982, *ApJ*, 252, 308
- Binney J., Tremaine S., 1987, *Galactic dynamics*
- Bournaud F., Jog C. J., Combes F., 2007, *A&A*, 476, 1179
- Cappellari M., Emsellem E., Bacon R., Bureau M., Davies R. L., de Zeeuw P. T., Falcón-Barroso J., Krajnović D., Kuntschner H., McDermid R. M., Peletier R. F., Sarzi M., van den Bosch R. C. E., van de Ven G., 2007, *MNRAS*, 379, 418
- Colín P., Valenzuela O., Klypin A., 2006, *ApJ*, 644, 687
- Combes F., 2009, in S. Jogee, I. Marinova, L. Hao, & G. A. Blanc ed., *Galaxy Evolution: Emerging Insights and Future Challenges* Vol. 419 of *Astronomical Society of the Pacific Conference Series*, Secular Evolution and the Assembly of Bulges. pp 31–+
- Combes F., Sanders R. H., 1981, *A&A*, 96, 164
- Davies R. L., Efstathiou G., Fall S. M., Illingworth G., Schechter P. L., 1983, *ApJ*, 266, 41
- Debattista V. P., Sellwood J. A., 2000, *ApJ*, 543, 704
- Dubinski J., Berentzen I., Shlosman I., 2009, *ApJ*, 697, 293
- Eggen O. J., Lynden-Bell D., Sandage A. R., 1962, *ApJ*, 136, 748
- El-Zant A., Shlosman I., Hoffman Y., 2001, *ApJ*, 560, 636
- Elmegreen B. G., Bournaud F., Elmegreen D. M., 2008, *ApJ*, 688, 67
- Erwin P., 2008, in M. Bureau, E. Athanassoula, & B. Barbuy ed., *IAU Symposium* Vol. 245 of *IAU Symposium*, The coexistence of classical bulges and disk pseudobulges in early-type disk galaxies. pp 113–116
- Evans N. W., 1993, *MNRAS*, 260, 191
- Fall S. M., Efstathiou G., 1980, *MNRAS*, 193, 189
- Franx M., Illingworth G., de Zeeuw T., 1991, *ApJ*, 383, 112
- Gadotti D. A., 2009, *MNRAS*, 393, 1531
- Gerhard O. E., Vietri M., Kent S. M., 1989, *ApJ*, 345, L33
- Hernquist L., Weinberg M. D., 1992, *ApJ*, 400, 80
- Holley-Bockelmann K., Weinberg M., Katz N., 2005, *MNRAS*, 363, 991
- Hopkins P. F., Bundy K., Croton D., Hernquist L., Keres D., Khochfar S., Stewart K., Wetzel A., Younger J. D., 2010, *ApJ*, 715, 202
- Hopkins P. F., Cox T. J., Younger J. D., Hernquist L., 2009, *ApJ*, 691, 1168
- Illingworth G., 1977, *ApJ*, 218, L43
- Immeli A., Samland M., Gerhard O., Westera P., 2004, *A&A*, 413, 547
- Jesseit R., Naab T., Burkert A., 2005, *MNRAS*, 360, 1185
- Katz N., Keres D., Dave R., Weinberg D. H., 2003, in J. L. Rosenberg & M. E. Putman ed., *The IGM/Galaxy Connection. The Distribution of Baryons at z=0* Vol. 281 of *Astrophysics and Space Science Library*, How Do Galaxies Get Their Gas?. pp 185–+
- Kauffmann G., White S. D. M., Guiderdoni B., 1993, *MNRAS*, 264, 201
- Kereš D., Katz N., Fardal M., Davé R., Weinberg D. H., 2009, *MNRAS*, 395, 160
- King I. R., 1966, *AJ*, 71, 64
- Kormendy J., 1982, *ApJ*, 257, 75
- Kormendy J., Illingworth G., 1982, *ApJ*, 256, 460
- Kormendy J., Kennicutt Jr. R. C., 2004, *ARA&A*, 42, 603
- Kuijken K., Dubinski J., 1995, *MNRAS*, 277, 1341
- Laurikainen E., Salo H., Buta R., Vasylyev S., 2004, *MNRAS*, 355, 1251
- Lynden-Bell D., Kalnajs A. J., 1972, *MNRAS*, 157, 1
- Marinova I., Jogee S., 2007, *ApJ*, 659, 1176
- Martinez-Valpuesta I., Shlosman I., 2004, *ApJ*, 613, L29
- Martinez-Valpuesta I., Shlosman I., Heller C., 2006, *ApJ*, 637, 214
- McMillan P. J., Dehnen W., 2007, *MNRAS*, 378, 541
- Méndez-Abreu J., Simonneau E., Aguerri J. A. L., Corsini E. M., 2010, *A&A*, 521, A71+
- Menéndez-Delmestre K., Sheth K., Schinnerer E., Jarrett T. H., Scoville N. Z., 2007, *ApJ*, 657, 790
- Mo H. J., Mao S., White S. D. M., 1998, *MNRAS*, 295, 319
- Morelli L., Pompei E., Pizzella A., Méndez-Abreu J., Corsini E. M., Coccato L., Saglia R. P., Sarzi M., Bertola

- F., 2008, MNRAS, 389, 341
- Nieto J.-L., Bender R., 1989, A&A, 215, 266
- Nowak N., Thomas J., Erwin P., Saglia R. P., Bender R., Davies R. I., 2010, MNRAS, 403, 646
- Pfenniger D., Norman C., 1990, ApJ, 363, 391
- Raha N., Sellwood J. A., James R. A., Kahn F. D., 1991, Nature, 352, 411
- Saha K., Tseng Y., Taam R. E., 2010, ApJ, 721, 1878
- Sellwood J. A., 1981, A&A, 99, 362
- Sellwood J. A., 2008, ApJ, 679, 379
- Sellwood J. A., Debattista V. P., 2006, ApJ, 639, 868
- Sellwood J. A., Evans N. W., 2001, ApJ, 546, 176
- Sellwood J. A., Valluri M., 1997, MNRAS, 287, 124
- Sellwood J. A., Wilkinson A., 1993, Reports on Progress in Physics, 56, 173
- Shen J., Rich R. M., Kormendy J., Howard C. D., De Propris R., Kunder A., 2010, ApJ, 720, L72
- Springel V., Hernquist L., 2005, ApJ, 622, L9
- Springel V., Yoshida N., White S. D. M., 2001, NewA, 6, 79
- Stark A. A., 1977, ApJ, 213, 368
- Toomre A., 1981, in S. M. Fall & D. Lynden-Bell ed., Structure and Evolution of Normal Galaxies What amplifies the spirals. pp 111–136
- Tremaine S., Weinberg M. D., 1984, MNRAS, 209, 729
- Villa-Vargas J., Shlosman I., Heller C., 2009, ApJ, 707, 218
- Weinberg M. D., 1985, MNRAS, 213, 451
- Weinberg M. D., Katz N., 2002, ApJ, 580, 627
- Weinberg M. D., Katz N., 2007a, MNRAS, 375, 425
- Weinberg M. D., Katz N., 2007b, MNRAS, 375, 460
- White S. D. M., Rees M. J., 1978, MNRAS, 183, 341
- Widrow L. M., Pym B., Dubinski J., 2008, ApJ, 679, 1239
- Zoccali M., 2010, in K. Cunha, M. Spite, & B. Barbuy ed., IAU Symposium Vol. 265 of IAU Symposium, The Stellar Population of the Galactic Bulge. pp 271–278
- Zoccali M., Hill V., Lecureur A., Barbuy B., Renzini A., Minniti D., Gómez A., Ortolani S., 2008, A&A, 486, 177